Received: 5 February 2020 | Revised: 30 March 2020 | Accepted: 30 March 2020

DOI: 10.1002/rcm.8803

Rapid Communications in Mass Spectrometry WILEY

RESEARCH ARTICLE

UV post-ionization laser ablation ionization mass spectrometry for improved nm-depth profiling resolution on Cr/Ni reference standard

Valentine Grimaudo[1] | Marek Tulej[1] | Andreas Riedo[1] | Rustam Lukmanov[1] | Niels F.W. Ligterink[2] | Coenraad de Koning[1] | Peter Wurz[1]

[1]Physics Institute, Space Research and Planetary Sciences, University of Bern, Switzerland

[2]Center for Space and Habitability, University of Bern, Switzerland

Correspondence
V. Grimaudo, Physics Institute, Space Research and Planetary Sciences, University of Bern, Sidlerstrasse 5, CH-3012 Bern, Switzerland.
Email: valentine.riedo@space.unibe.ch

Funding information
Swiss National Science Foundation

Rationale: Laser ablation combined with mass spectrometry forms a promising tool for chemical depth profiling of solids. At irradiations near the ablation threshold, high depth resolutions are achieved. However, at these conditions, a large fraction of ablated species is neutral and therefore invisible to the instrument. To compensate for this effect, an additional ionization step can be introduced.

Methods: Double-pulse laser ablation is frequently used in material sciences to produce shallow craters. We apply double-pulse UV femtosecond (fs) Laser Ablation Ionization Mass Spectrometry to investigate the depth profiling performance. The first pulse energy is set to gentle ablation conditions, whereas the second pulse is applied at a delay and a pulse energy promoting the highest possible ion yield.

Results: The experiments were performed on a Cr/Ni multi-layered standard. For a mean ablation rate of ~3 nm/pulse (~72 nJ/pulse), a delay of ~73 ps provided optimal results. By further increasing the energy of the second pulse (5–30% higher with respect to the first pulse) an enhancement of up to 15 times the single pulse intensity was achieved. These conditions resulted in mean depth resolutions of ~37 and ~30 nm for the Cr and Ni layers, respectively.

Conclusions: It is demonstrated on the thin-film standard that the double-pulse excitation scheme substantially enhances the chemical depth profiling resolution of LIMS with respect to the single-pulse scheme. The post-ionization allows for extraordinarily low ablation rates and for quantitative and stoichiometric analysis of nm-thick films/coatings.

1 | INTRODUCTION

Understanding of the chemical composition at surfaces and below, i.e., depth profiles at very localized areas on the sample is of high interest in multiple disciplines. The field of application ranges from the semiconductor industry, which, amongst others, is interested to evidence possible impurities within high purity functional materials to improve their interconnect technology,[1,2] and the integrity of chemical interfaces, to geochemical and geochronological analysis in space and planetology research, where the elemental and isotope constitution of a heterogeneous specimen provides relevant information about ongoing evolutionary planetary processes.[3,4] Many functional materials have particular chemical and physical properties associated with specific surface-confined thin films that differ from the bulk material. Because of their characteristic chemical composition, which determines their application, knowledge of chemical depth profiles is of importance to control their manufacturing and to ensure the reliability and performance of the end product.

Various well-established sensitive spectroscopic measurement techniques that probe the surface and near-surface volume can

provide valuable insights into the surface composition, e.g., X-ray Photoelectron Spectroscopy (XPS), Auger Electron Spectroscopy (AES) or Raman microspectroscopy (micro-Raman), just to mention a few. In XPS, the kinetic energy of emitted electrons originating from the 20–30 uppermost monolayers resulting from the irradiation with soft X-rays (~1200–1500 eV) is analyzed.[3,5] AES is based on the analysis of emitted Auger electrons from about the uppermost 0.5 nm that are formed when core vacancies generated by irradiation with energetic electrons or X-ray (photoelectrical effect) are replaced by electrons from higher energetic levels.[3,5] In micro-Raman, the frequency shift of an incident monochromatic light beam through inelastic scattering on the surface is monitored, which provides chemical and structural information of vibrational states with micrometer spatial resolution.[3,6]

These techniques differ in their strengths, which involve either the spatial resolution, detection sensitivity, or quantification of species. As a result, a combination of these techniques is typically required to solve a specific question for a given research topic. One shared characteristic of each of the mentioned techniques is that they are constrained to the topmost layers. To profile a film of several micrometres entirely, they typically need to be combined with an ion gun for sputtering of the residual surface, which influences and limits the achievable depth resolution through atomic-mixing and surface roughening and drastically increases the measurement time and cost.[7]

One of the most advanced and applied techniques in microelectronics and Earth sciences is Secondary Ion Mass Spectrometry (SIMS), which is based on the bombardment of a surface with primary ions and the subsequent ejection of charged particles (secondary ions) from the analyte.[3,8] In static mode (e.g., time-of-flight (TOF)-SIMS), the current of the incoming ion beam is kept low and only little surface damage is induced. In this way, SIMS provides elemental and molecular information of the uppermost two monolayers. In contrast, dynamic mode causes rapid surface erosion with an increased ion flux of the primary ion beam (e.g., Nano-SIMS) and elemental mapping and depth profiling measurements can be conducted. In particular Nano-SIMS has emerged as an important tool for microprobe analysis, because it provides very high lateral resolution (~50 nm), trace element analysis, isotope ratio analysis, and three-dimensional (3D) chemical imaging. However, it is limited in terms of the number of simultaneously detectable mass-to-charge (m/z) ratios.[3] Another important drawback of SIMS in general is the strong dependence of the ion yield on the chemical environment of the sputtered area. Because of this matrix effect, a quantitative, and in some cases even qualitative, assessment becomes impossible if no appropriate matrix-matched standard reference sample is available.[9]

Spatially coherent and focused laser irradiation for the ablation of material is a promising alternative to the ion beam erosion in SIMS to probe material in depth, especially when using ultra-short (< ps) laser pulses. Laser pulse widths in the time scales below the material vibrational time scale (phonon frequencies) have a number of advantages. They induce minimal spatial thermal damage on the irradiated zone and avoid interaction and reheating of the ejected material by the trailing edge of the pulse (laser-plasma interaction).[10] When using femtosecond (fs) laser pulses, the surface irradiation and ablation plume formation are separated, which further avoids element fractionation as is induced by nanosecond pulses. Hence, using fs laser pulses improves the elemental composition analysis of the investigated solid, allowing nearly stoichiometric ablation, atomization, and ionization of the elements comprising the solid material.[11,12] Laser Ablation Inductively Coupled Plasma Mass Spectrometry (LA-ICP-MS) is a widely applied method for quantitative assessment of trace, minor, and major elements in solids.[13,14] State-of-the-art instruments report figures of merits that involve detection sensitivities down to the parts-per-billion (ppb) level[15] and lateral and depth resolution in the micrometer and nanometer range, respectively. While these figures of merit constitute a clear advantage, LA-ICP-MS suffers from several significant drawbacks. Examples of these include element fractionation related to the ablation process depending on the used laser system, and unwanted contributions of the aerosol transport process from the ablation chamber into the ICP, as well as from the vaporization, atomization, and ionization process in the ICP itself. These factors complicate the entire analysis and demand tailored calibration concepts.[15]

Another technique using laser ablation (LA) with broad application in standard laboratory-based chemical analysis is Laser-Induced Breakdown Spectroscopy (LIBS). This technology, which measures characteristic optical emission lines of neutral atoms and ions from the laser plasma plume after their decay from an excited state to a lower energy level, provides the opportunity to inspect the chemical composition of distant or even submerged solid objects.[16] The remote sensing application permits the chemical investigation of solids in challenging environments without the need of any sample pretreatment. LIBS is, for example, deployed in the Mars Science Laboratory Mission led by the NASA Mars Exploration Program.[17] The success of such measurements, however, depends greatly on the propagation of light (laser and emission) through the atmosphere, e.g., atmospheric turbulences, and on the spectral lines considered. Furthermore, this technique suffers from sensitivities limited to the ‰-level for many elements of interest. This is induced in part by the detector characteristics of the spectrometers and in part by the detectable optical emission (e.g., emission in the ultraviolet (UV) regime and in time scales that are very close to the temporal resolution of the CCD/ICCD detectors), which require a certain minimum of laser fluence and therefore limit the achievable spatial resolution for depth profiling experiments. To compensate for these disadvantages, much effort has been focused on developing new methods to enhance spectral emission intensity and plasma persistence by the implementation of, e.g., a double-pulse (DP) laser system,[18–21] a high-voltage electrical pulse,[22] a microwave,[23] or a glow discharge[16] excitation source in the LA process.

In addition to the aforementioned limitations concerning elemental fractionation, all LA-based techniques are, to a certain extent, contingent on the chemical and physical properties of the sample itself. Although matrix effects are minimized by employing

ultra-short laser pulses, there can be spatial dependencies of the ablation due to chemical or physical inhomogeneities with dimensions exceeding the laser spot size, e.g., the immiscibility of components in the analyte. Such a constitution of the analyte influences the material removal rate and introduces uncertainties with respect to the allocation of the depth scale in depth profiles. In addition, all techniques applying erosion procedures that include particle or light beams to probe a depth profile have in common that with time an increasing surface roughening occurs, which promotes to a certain extent the atomic mixing of sublayers, and consequently restricts the achievable vertical resolution. This effect is intensified by so-called side-wall contributions of induced craters with high depth-to-diameter aspect ratios.[24,25]

Furthermore, when using detection systems that measure ionized species directly without the application of an additional ionization source (e.g., ICP), working at the ablation threshold can impair the signal-to-noise ratio of the monitored element, i.e., if the threshold for its neutral state is attained but not its ionization level. When no additional ionization step is involved subsequent to ablation, higher fluences need to be applied to reach the ionization level, which implies lower depth resolutions.

In this work, we employ a collinear (same axis of propagation) depth profiling laser system with two temporally separated pulses for the Laser Ablation Ionization Mass Spectrometry (LIMS) technique with our miniature reflectron-type TOF mass analyzer designed for space applications.[12,26–29] The implemented double-pulse (DP) method increases the ionization efficiencies of the LA process, which results in higher spatial resolution in depth profiling experiments. For this, an additional beam guiding system consisting of a variable retroreflector system is implemented in the optical beam path of the laser to create a second laser pulse with an adjustable delay in the picosecond regime. The first laser pulse is tuned to optimize the ablation of material from the sample, the second, delayed pulse is absorbed by the ejected material, which heats the plasma plume, and optimizes the atomic ion yield prior to mass spectrometric analysis. Several publications have appeared on the theoretical understanding of DP ablation and several experimental studies were conducted to understand plasma plume dynamics.[30–33] In this study, a similar beam guiding system was employed as in an earlier study, where DP IR fs-laser radiation was employed.[34] Based on measurements conducted on a thin-layer depth profiling standard reference material (NIST SRM 2135c), we demonstrate that the quality of the depth profile can significantly be improved by applying DP ablation.

2 | EXPERIMENTAL

2.1 | Sample material

The state-of-the-art reference standard SRM 2135c (NIST, Gaithersburg, MD, USA) for DP measurements consisting of nine alternating Cr/Ni layers (5 × Cr and 4 × Ni) with nominal layer thicknesses of 57 nm and 56 nm for Cr and Ni, respectively, was used in this study. These nine alternating layers are accommodated on a Si wafer substrate (see Figure 1).

2.2 | Laser ablation ionization mass spectrometer

A detailed description of the instrumentation can be found in our earlier publications.[12,35–37] Only a brief overview of the mass spectrometric system is given here.

The mass analyzer of the instrument is a miniature reflectron-type time-of-flight (R-TOF) mass spectrometer that is located inside a vacuum chamber at pressure <10^{-7} mbar. The ablation ion source is a Chirped Pulse Amplified (CPA) laser system (Clark-MXR Inc., Dexter, MI, USA) that generates pulses of ~190 fs pulse width at 1 kHz laser pulse repetition rate and 258 nm wavelength, after harmonic conversion (Storc, Clark-MXR Inc.) from the fundamental at 775 nm. A dedicated optical system consisting of dielectric mirrors (e.g., Thorlabs Inc., Newton, NJ, USA) and beam expander (Eksma Optics, Vilnius, Lithuania) guides the laser pulses towards the chamber, through an entrance window, then through the mass analyzer, and along its central axis, down to the sample, which is positioned right below the entrance ion optics of the analyzer. The sample surface is remotely manipulated by a x,y,z-translation stage with micrometer positioning accuracy at the focal plane of the laser beam. The focal plane is investigated once, at the beginning of the measurement campaign, by online monitoring of the signal intensity and the crater size for very low pulse energies. At these laser conditions, a clear signal and crater are only observed when the sample surface is located at the focal point. The ion-optical system transmits only positively charged species towards the detection unit, which consists of two microchannel plates (MCPs) in a chevron configuration and four centrosymmetric anodic rings.[36] However, in this study, only one of the four anodes was used for the detection of the ion current. The signal is recorded by a high-speed ADC data acquisition system (U5303A, Acqiris SA, Geneva, Switzerland) with a sampling rate of 3.2 GS/s and a dynamic range of 12 bit.

The DP unit consists of two beam splitters (50/50 transmission/reflection) used for the separation and recombination of the two laser pulses, as well as other optical elements, e.g., Al-coated mirrors to guide the pulses towards the sample. The first beam splitter divides the beam into a static and variable beam guiding system. The variable guiding system consists of a movable retroreflector system

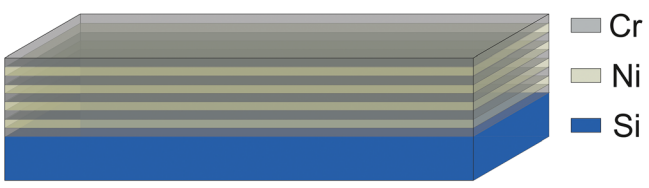

FIGURE 1 Schematic drawing of the standard reference sample NIST SRM 2135c [Color figure can be viewed at wileyonlinelibrary.com]

that is positioned on a 300 mm long remote-controllable linear motorized microtranslation stage (Zaber Technologies Inc., Vancouver, Canada), which serves to adjust the delay of the second pulse (ps to ns delay, 600,000 possible positioning steps). Note that the zero delay between the two laser pulses was within the 300 mm movable stage and not at one end. This configuration allows the user to select which laser pulse reaches the sample surface first. Moreover, special attention was paid to ensure that the two laser pulses had a similar beam profile. The pulse energy of each beam is adjusted by a motorized attenuator system consisting of a half-wave plate and a polarizer system (Newport, Irvine, CA, USA), which precisely controls the laser attenuation in fine steps. The second beam splitter combines the two beams before a harmonic generator system, where the fundamental wavelength is converted to 258 nm. From this point, both pulses follow the same beam path, which guides the pulses through a beam expander to the vacuum chamber. Figure 2 shows a schematic overview of the DP unit. For the automation of the entire instrument (laser system, data acquisition, sample stage and delay stage) we use in-house written software.

2.3 | Measurement procedure

In all measurement campaigns, the applied voltage difference over the MCPs in the detector unit was set between 1450 and 1500 V and single laser shot mass spectra were recorded at 1 kHz repetition rate. The gain of the data acquisition system was set to 1 V with an offset value of +0.47 V. Note that this offset is required to use the full 12-bit dynamic range of the measurement cards, since it records a negative signal. The ion signal was acquired with a sampling rate of 3.2 GS/s giving 64,000 samples for 20 µs recording time per TOF spectrum. The energy of the UV pulses was measured before and after each measurement with a J-10 MB-LE sensor (Coherent, Santa Clara, CA, USA) by averaging 10,000 pulses just in front of the beam expander. The base pressure inside the vacuum chamber was in the range of $(2–4) \times 10^{-8}$ mbar. This pressure is sustained by an ion getter pump to avoid any vibrations coming from the turbo-molecular pumping system, including its roughing-pump (scroll pump), which is only used for the initial pump down procedure of the system during system maintenance. All measurements were conducted on the state-of-the-art depth profiling NIST standard 2135c. The following list details each conducted measurement step to achieve optimal measurement conditions for the depth profiling of the NIST standard:

i. Mean ablation rate: Each data point is a mean of five measurements, each consisting of 500 single laser shots. The campaign was conducted using the static beam only, by blocking the variable beam.
ii. DP raster campaign: The optimal pulse delay was probed by moving the retroreflector from the variable beam guiding system 400 times in steps of ~0.6 ps in the same direction starting slightly before the zero delay to ~240 ps. Each delay was probed on a new location on the sample surface by programming a raster campaign of 20×20 craters with a 30 µm pitch. For each measurement, 500 single laser shots were recorded. Both beam guiding systems were set to ~72 nJ/pulse using the variable attenuators.
iii. Pulse energy adjustment of the delayed pulse (second pulse): The stage of the movable retroreflector was set to an optimal pulse delay timing of ~73 ps. The first pulse was set to a constant pulse energy of ~72 nJ/pulse, while the energy of the second pulse was varied between about 72 nJ and 123 nJ. Note, the first pulse reaching the surface is again set to the same energy as in experiment part (ii), since this first pulse determines the ablation rate and therefore the amount of ablated material in the plume. Only the delayed pulse is increased in pulse energy, which is absorbed by the ablation plume. Small discrepancies of the ablation rate arose from external factors, e.g., the motion of the sample with respect to the laser beam induced by external vibrations. Each measurement consisted of 500 single laser shots

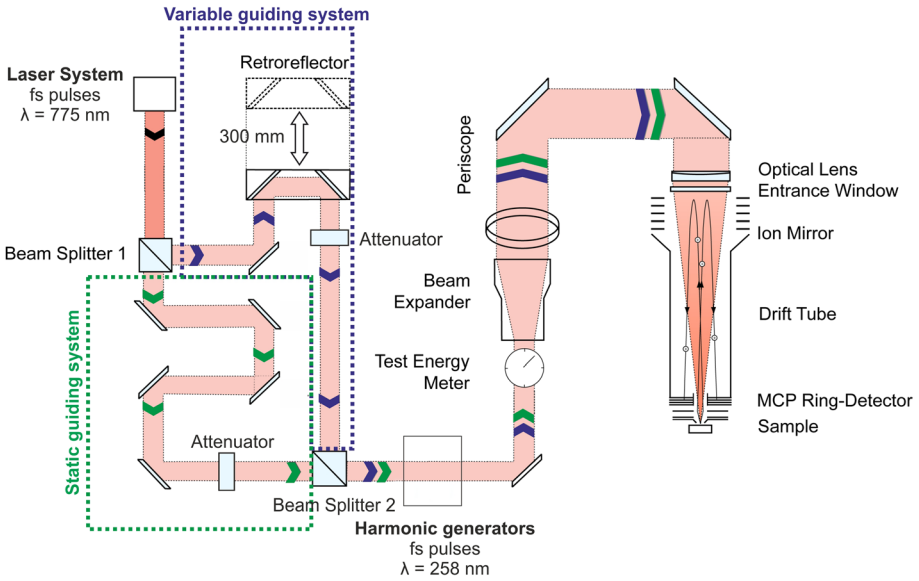

FIGURE 2 Schematic overview of the double-pulse (DP) unit [Color figure can be viewed at wileyonlinelibrary.com]

and was repeated five times, with each measurement being conducted on a new (fresh) position.

iv. Proof of concept – depth profile of standard reference material NIST SRM 2135c: For each tested pulse energy in (iii), a full depth profiling measurement, consisting of single-shot mass spectra, was recorded.

3 | RESULTS AND DISCUSSION

To achieve optimal parameters for chemical depth profiling measurements, preparatory experiments need to be conducted, i.e., the up-take rate of the ablation has to be adjusted adequately to obtain the desired depth resolution for the chemical analysis. Therefore, the correlation between the amount of ablated material and the applied pulse energy was investigated first. To avoid any contribution from the second laser pulse, its beam path was blocked. Next, the mean ablation rate is calculated for a certain range of pulse energies by recording the number of laser pulses required to ablate all Cr and Ni layers completely, as indicated by the onset of the Si ablation from the substrate. All measurements were repeated five times for statistical relevance.

Using a UV fs laser beam, only tens of nJ per pulse and a few hundred consecutive pulses are required to ablate about 500 nm of metallic sample material. The measurements show that by reducing the pulse energy, the mean up-take rate is reduced to several nm per laser pulse, while still staying above the threshold for ablation of the corresponding materials (Cr/Ni/Si). Note that Figure 3 represents a mean ablation rate comprising the ablation of both metals (Cr and Ni) based on the onset of the Si-substrate. The ablation threshold for Cr and Ni is lower than for Si because of the intrinsic electronic property of these metals. Therefore, we expect that there is still room for improvement in the depth profiling resolution of the Cr/Ni layers.

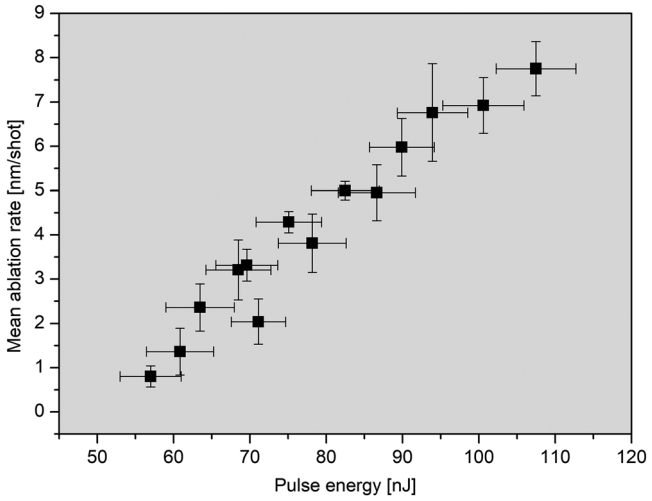

FIGURE 3 The mean ablation rate for single-pulse operation at different pulse energies based on the onset of the Si-substrate signal after completely ablating all Ni and Cr layers in NIST SRM 2135c. Each data point represents a mean of five ablation measurements

However, to prove the concept of this new methodology, a moderately low pulse energy was chosen for the continuation of the experiment. About 72 nJ, which was clearly above the ablation threshold for Si, was chosen as pulse energy for the following experiments. This pulse energy resulted consistently in a mean up-take rate of about 3 nm per laser pulse.

Using this pulse energy, the effect of varying pulse delays on the ionization efficiency of the ablated material was investigated. For this experiment, the second beam path was opened and its length was extended by 0.0875 mm at each step, corresponding to an increase of about 0.6 ps per step. Around a delay of $t = 0$ s, the two pulses overlap and the resulting pulse energy on the sample surface is doubled. This is seen at the beginning of the intensity profile in Figure 4A by an abrupt signal increase. The signal for Ni and Cr is the sum of all the isotope peak areas in each single TOF spectrum. Figure 4B exemplifies by means of laser-induced craters on a steel sample the impact of overlapping pulses in time. Craters formed with almost perfect time overlap (t ~0 s) are situated in the center of the raster campaign. With increasing delays, the second pulse is shielded by the ablated plume and does not reach the sample surface anymore. Around a delay of 73 ps (estimated from the turning point in Figure 4A), the photon package of the second pulse is well absorbed by all species in the ablation plume, heating the plasma plume, ionizing atomic neutrals and atomizing cluster fraction ablated from the sample material. Note that this delay depends on the applied pulse energy and on the physical and chemical properties of the material. The additional ionization becomes most evident when pulse energies near the ablation threshold of the material are applied. Near the ablation threshold, the majority of the ablated species are neutrals,[38] which can be non-resonantly ionized by the second pulse. This results in a measurable increase in the recorded ion intensities and thus in an enhancement of the measurement sensitivity without ablating more sample material.

The ion yield can be enhanced further without affecting the ablation process by optimizing the second, delayed, pulse energy. The energy of the first pulse, which defines the up-take rate in the ablation process, was kept constant to maintain constant depth resolution. The larger photon intensity in the second pulse increased the ionization of the material ablated by the first pulse.

As depicted in Figure 5, the mean ablation rate was not affected by the increased energy of the second, post-ionizing pulse, up to approximately 90 nJ. The ablation rate for a single pulse (SP) is represented by the asterisk symbol and is about 3 nm/shot. Above a pulse energy of 90 nJ (note: the first laser pulse is kept at an energy of 72 nJ/pulse), the second pulse starts to contribute to the ablation process. Thenceforth, each additional energy contribution resulted in an increase in the ablation rate.

The signal intensity was calculated by summing the recorded TOF peak areas of Cr and Ni isotopes for each single-shot spectrum, up to the onset of the Si-substrate, and subsequently normalizing the cumulative value to the corresponding number of applied laser pulses to reach the Si onset. For elevated energies of the second pulse, the increasing intensity trend flattens out. This might be (in part) due to

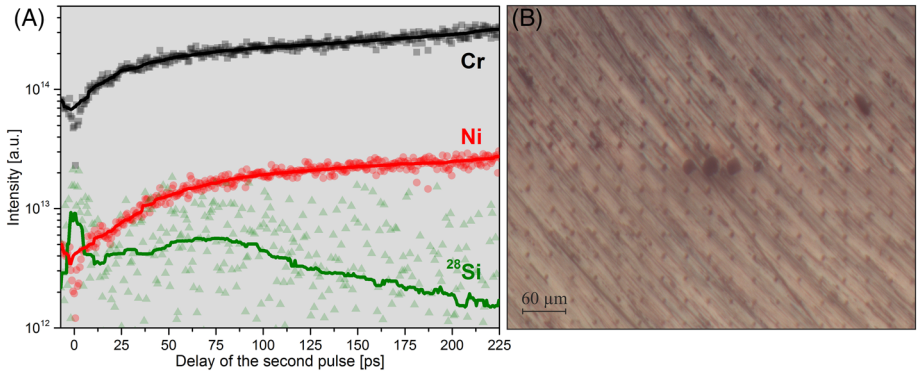

FIGURE 4 A, Intensity profile of Cr, Ni, and ^{28}Si for varying time separations between the two pulses. Both pulses were set at ~72 nJ. Each data point consists of an accumulation of 500 single laser shots recorded on a fresh surface position. Around a delay of 73 ps efficient ionization of all species in the ablation plume was obtained. B, Crater array after DP ablation on a steel sample, with each crater formed at a different delay of the second pulse. The effect of overlapping laser pulses at pulse delays around t = 0 s is seen as significant intensification of the crater size in the centre of the array [Color figure can be viewed at wileyonlinelibrary.com]

optimal ionization being achieved at a certain combination of first pulse and second pulse energy. Increasing the second pulse energy past this point does not contribute to a measurably higher degree of ionization within the produced plume. When the maximum ionization degree is reached, the excess energy from the second pulse is absorbed by the underlying material, where it causes effects similar to the first pulse (mainly ablation, less ionization). The differences between the SP (asterisk symbols) and DP (square symbols) measurements are remarkable. At a similar mean ablation rate, much higher signal intensity is observed when the delayed pulse is allowed to reach the plume than in SP experiments. In Figure 5 one can see an

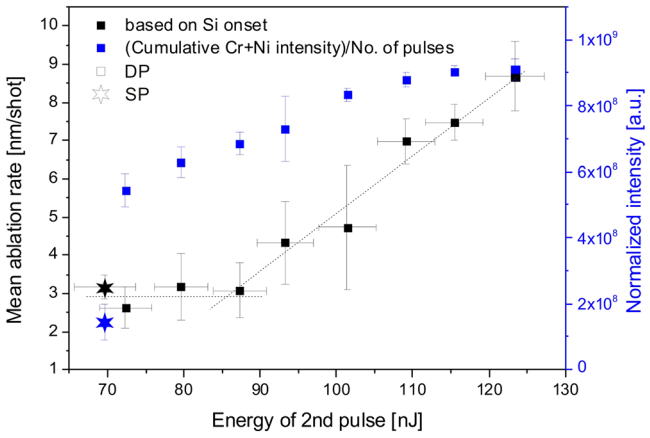

FIGURE 5 Dependence of the energy of the delayed pulse on the mean ablation rate and ion intensity. Each measurement point is a mean of five measurements with 500 single laser shots. Above a certain pulse energy, the delayed pulse starts to contribute to the ablation process. The asterisk symbols represent the SP measurements, and the square symbols the DP measurements. The energy of the first pulse (or SP) is kept at 72 nJ. The blue data points belong to the right y-axis and constitute the sum of all Cr and Ni isotope peak areas for each measurement up to the Si-onset. These values are normalized to the number of pulses required to reach the substrate [Color figure can be viewed at wileyonlinelibrary.com]

increase in the summed Cr and Ni intensities by a factor of almost 4. This value is dominated by the Cr signal. The Ni signal is less intense; however, the DP has a stronger influence on that element. This clearly demonstrates the impact of the post-ionization step on the signal-to-noise ratio (SNR).

The impact of the DP system on the depth profiles is illustrated in Figure 6 on the basis of different configurations. This figure shows the Cr signal in the top panels, the Ni signal in the middle, and the Si-signal onset from the substrate at the bottom. The SP profiles are presented in Figures 6A–6C. When employing the SP system, the five Cr layers are discernible, but the SNR for Ni is too low to recognize clearly structural changes within the reference material. The poor profiling quality in the case of the SP is only because too few ions are being produced at the applied pulse energy, since most material is removed as neutrals. Figures 6D–6F show the depth profiles when performing DP measurements with the two pulses set at an identical energy to the single pulse of the SP experiment, and with no time shift (delay = 0 s) between the two pulses. In this configuration the total energy reaching the surface was basically twice as high as in the case of the SP experiment. Accordingly, only about half of the number of pulses was required to reach the Si-substrate, which reduced the depth resolution. However, through the larger irradiances, increased ionization of the ablated material and therefore larger signals were measured. In Figures 6G–6I and 6J–6L, the two pulses were separated by about 73 ps. In the case of the measurements presented in Figures 6J–6L, the pulse energy of the delayed pulse was raised to slightly higher values relative to the first pulse. Note that, for the measurements presented in Figures 6A–6C, 6G–6I and 6J–6L, the ablation process was determined only by one (the first) pulse, which was kept at constant conditions (energy, width, and wavelength), and so the up-take rates were uniform for all three experiments.

The DP system increases ionization and thus sensitivity and, as a result, the instrument becomes sensitive enough to resolve the expected periodic fluctuations in Ni and Cr. The depth profiles

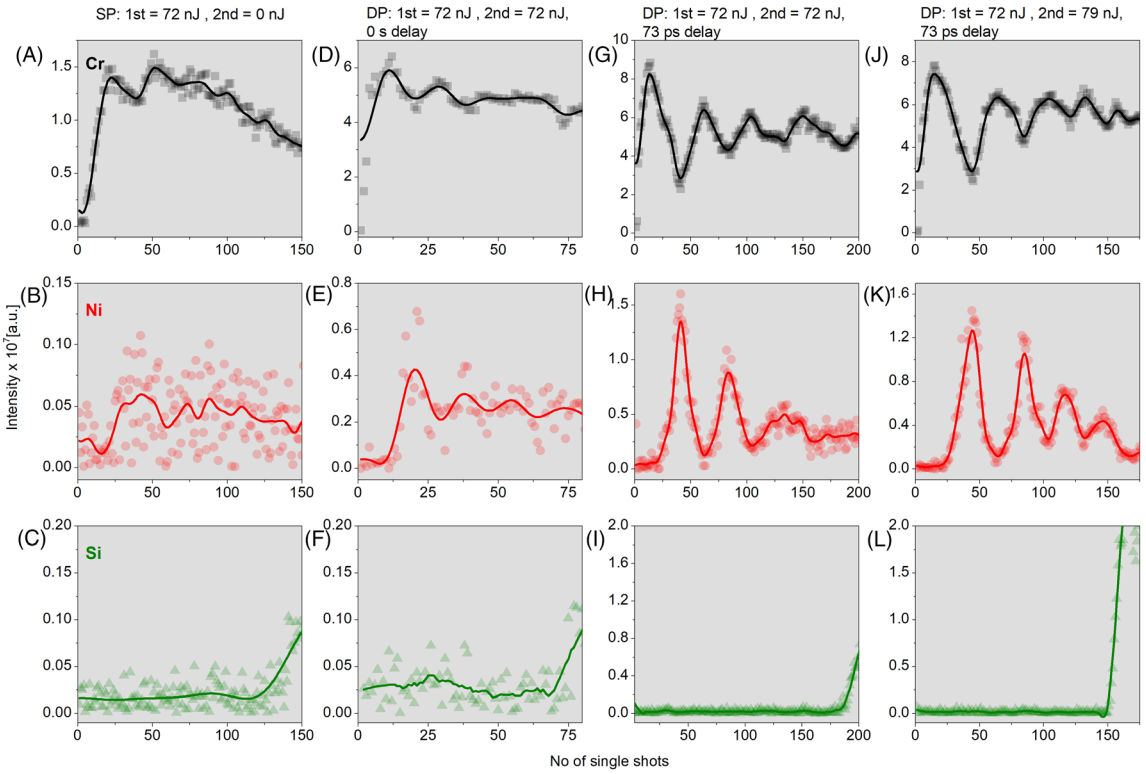

FIGURE 6 Comparison of A–C, a single pulse (SP); D–F, a double pulse (DP) with both pulses at the same energy (72 nJ) and 0 s delay; G–I, a DP with both pulses at the same energy (72 nJ) and ~73 ps delay; and J–L, a DP with the first pulse at 72 nJ, the second pulse at 79 nJ, and ~73 ps delay. Top, middle and bottom panels describe the recorded depth profiles of Cr, Ni and Si, respectively. The figure clearly shows an improvement in the depth profiles with the implementation of the DP and the right delay, and with the increased energy of the second pulse (J–L) [Color figure can be viewed at wileyonlinelibrary.com]

displayed in Figures 6H and 6K show an enhancement of the Ni signal of a factor of about 15. The enhanced ionization by the DP can improve the resolution of the chemical depth profiles significantly by allowing for a low first pulse energy, and thus a decreased ablation rate. Note that the applied pulse energy for the ablation of Ni and Cr was set to a value where a clear ablation of the Si-substrate was observed (Figure 3), which is expected to be far above the ablation threshold for the Cr and Ni metals.

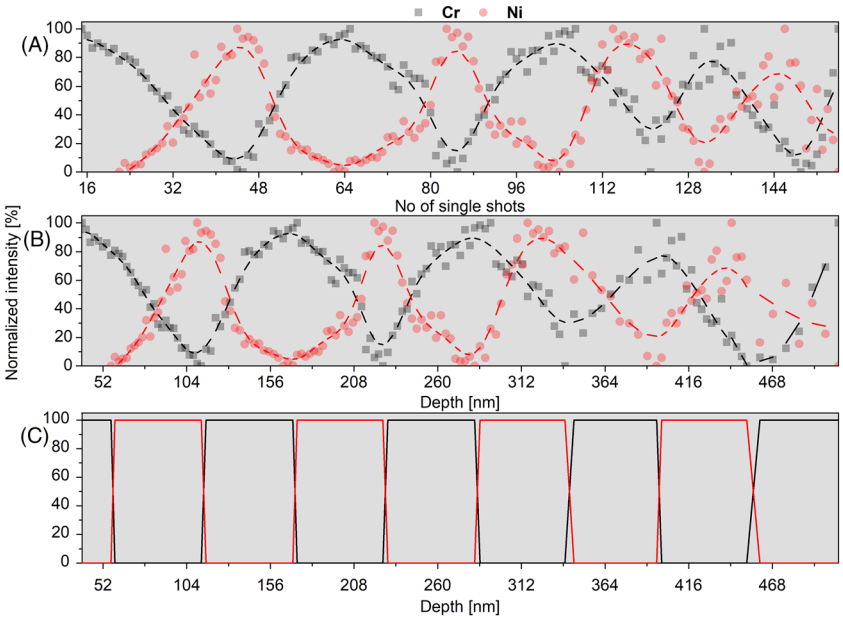

FIGURE 7 Cr and Ni depth profiles A, with the number of applied laser shots and B, with the depth in nm. Each layer is normalized according to its highest and lowest signal. The profiles are smoothed with a five-point Fast Fourier function shown as dashed lines on the data. C, Rectangular step functions, derived from the Cr and Ni signal increase and decrease of each layer. The step functions illustrate the constant and uniform ablation rate along the sample depth up to the last two layers of the reference standard [Color figure can be viewed at wileyonlinelibrary.com]

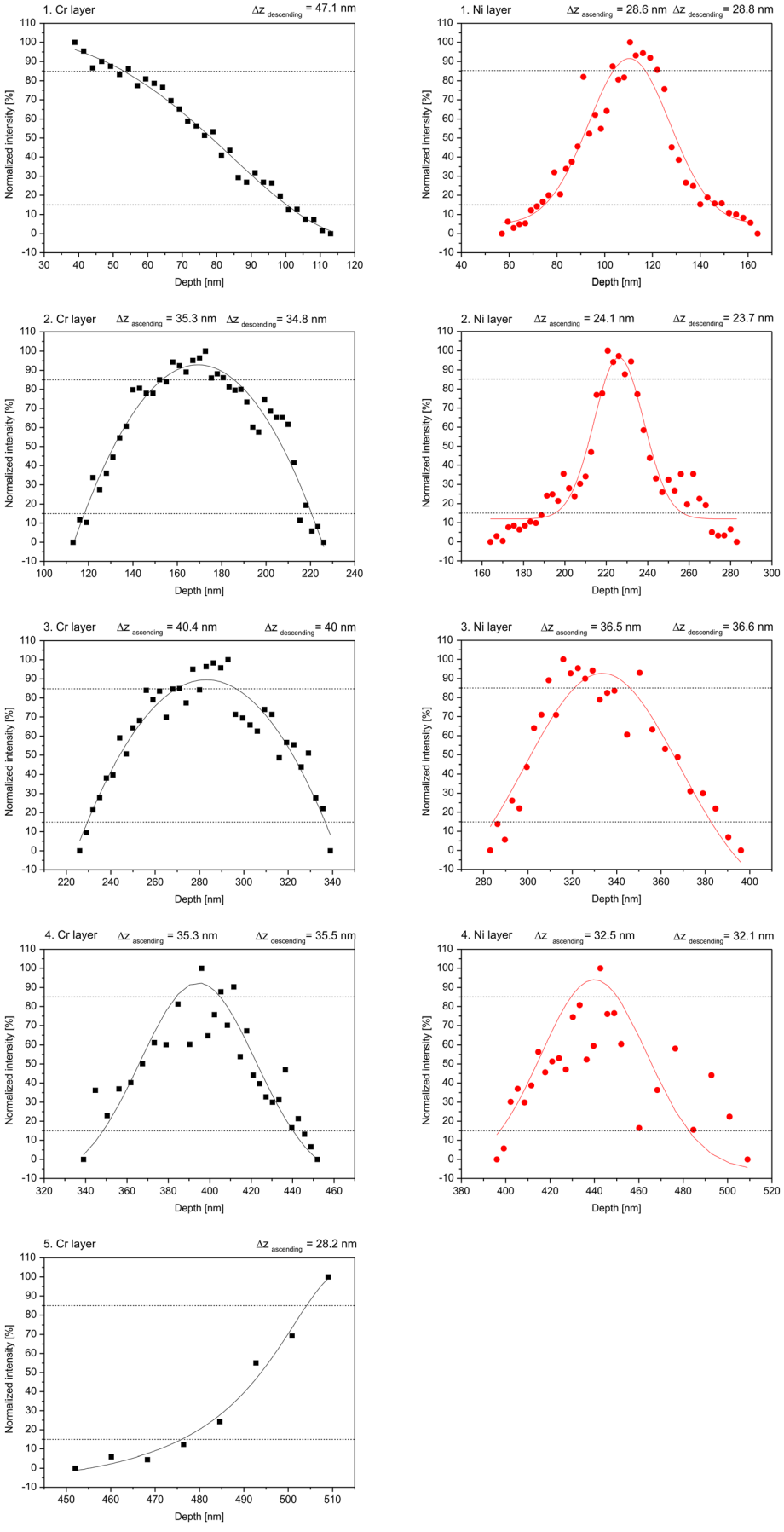

FIGURE 8 Depth resolution (Δz) of each metal layer for the ascending and descending shoulder of the recorded depth profiles. All profiles, except for the 5th Cr layer, are fitted by a Gauss Amplitude Function, whereas a Lorentz Function was used in case of the last Cr layer. The 84% and 16% intensity margins, from which the Δz values are derived, are emphasized by the horizontal dotted lines [Color figure can be viewed at wileyonlinelibrary.com]

Figure 7 illustrates the capability of the DP measurement to reproduce the layer structure of the sample, using the raw data presented on the rightmost columns of Figures 6J–6L. In Figure 7, the depth profiling intensity for each metal is corrected for the known decrease in signal intensity with depth, and for the increased baseline resulting from increasing side-wall contributions with depth.[7,39–41] These corrections were easily derived from the highest and lowest points of the recorded signal for every recorded layer. Figure 7A shows the progression of the normalized signal intensity with the number of applied single laser shots. In Figure 7B, the laser shot number was converted into a depth scale, by considering the mean ablation rate for each layer, which was derived from the signal onset of the following metal layer. Figure 7C illustrates the monotonic alteration of the Cr and Ni signals by means of rectangular step functions and indicates the uniform ablation of both metals.

In Figure 8 the normalized depth profiles of each layer shown in Figure 7B are fitted by a Gauss Amplitude function, except for the last Cr layer, which is fitted by a Lorentz function. From these fits we derived the depth resolution. The most frequently used definition for depth resolution in sputtering profiles of multilayer structures denotes the depth resolution as the distance on the depth scale between the intensity value of 84% and 16% of the most intense signal of the corresponding layer (84% and 16% margin are indicated by horizontal dotted lines in the panels of Figure 8).[40,42] Except for the first and last Cr layers, two values for each layer were determined, similar to Käser et al, describing the depth resolution (Δz) of the ascending and descending shoulder of the recorded profile.[42]

In agreement with the literature, where a lower ablation threshold for Cr than for Ni is reported,[43,44] lower depth resolutions are observed for Cr than for Ni while applying the same energy per pulse. The single-shot ablation threshold fluences are reported in the literature to be 0.19 J/cm^2 for Cr[43] and 0.41 J/cm^2 for Ni.[44] The mean depth resolution for the ascending shoulder was found to be ~37 nm for Cr and ~30 nm for Ni.

The different peak shapes of Cr and Ni might arise from the different physical and chemical nature of the two metals, e.g. melting point and ionization energy.

Based on the current improvements in the ionization efficiency with the DP method, LIMS is now reaching a slightly better depth profiling performance than state-of-the-art laser ablation instruments.[42] It is important to note at this point that no pulse-shaping device for flat-top profiles is used in our LIMS system. Flat-top laser profiles might be of greater relevance for the analysis of thicker layers, in the rage of tens of micrometers thickness, due to the formation of conical crater shapes when using Gaussian pulses.[45] Note that the derived depth resolutions were obtained at a moderately low pulse energy (inducing mean ablation rate of 3 nm/shot) and do not represent the limit of instrument performance. The initial ablation studies (Figure 3), as well as earlier studies carried out with an IR laser,[46] have shown the capability to reach mean material up-take rates of <1 nm per pulse. By decreasing the initial pulse energy even below the threshold for ablation of ionized species, higher depth resolutions are expected to be achieved, because the threshold for neutral species ablation is typically at distinctly lower energies.

4 | CONCLUSIONS

Within the framework of this study, we have demonstrated vast improvement in the depth profiling capabilities of our LIMS system on the depth profiling standard reference sample NIST SRM 2135c by extending the optical path of the laser system with a variable beam guiding system. The dynamic beam guiding system introduces a delay of several picoseconds between split pulses and allows for efficient post-ionization of neutral species in the ablated plume. Because of the mild ablation conditions applied, the ablation plume consists to a major extent of neutral species. With these instrument modifications, the signals for Ni and Cr could be increased by a factor of about 15 and 5, respectively, and all individual Ni and Cr metal layers, each of about 60 nm thickness, could be resolved separately without the need for any data treatment. From a detailed analysis, we found that for the applied conditions the mean depth resolutions were ~30 nm for Ni and ~37 nm for Cr. Moreover, the up-take rate of the metal layers was not tuned to the possible minimum. We expect to significantly improve the depth resolution by further decreasing the pulse energies below the ablation threshold of the Si-substrate. In agreement with the SP ablation rate campaign, where the lowest tested pulse energy (57 nJ) resulted in 3 times lower mean ablation rates than the applied pulse energy in the DP campaign, a depth resolution of at least 3 times higher (Δz ~10 nm) is expected to be achievable.

ACKNOWLEDGEMENT

This work was supported by the Swiss National Science Foundation.

ORCID

Valentine Grimaudo https://orcid.org/0000-0002-7010-5903
Andreas Riedo https://orcid.org/0000-0001-9007-5791
Niels F.W. Ligterink https://orcid.org/0000-0002-8385-9149

REFERENCES

1. Reid JD, Zhou J. Impact of leveler molecular weight and concentration on damascene copper electroplating. *ECS Trans*. 2007;2(6):77-92.
2. Lühn O, Van Hoof C, Ruythooren W, Celis JP. Filling of microvia with an aspect ratio of 5 by copper electrodeposition. *Electrochim Acta*. 2009;54(9):2504-2508.
3. Qian G, Li Y, Gerson AR. Applications of surface analytical techniques in earth sciences. *Surf Sci Rep*. 2015;70(1):86-133.
4. Kelly CJ, McFarlane CRM, Schneider DA, Jackson SE. Dating micrometre-thin rims using a LA-ICP-MS depth profiling technique on zircon from an Archaean Metasediment: Comparison with the SIMS depth profiling method. *Geostand Geoanal Res*. 2014;38(4):389-407.

5. Reniers F, Tewell C. New improvements in energy and spatial (x, y, z) resolution in AES and XPS applications. *J Electron Spectrosc Relat Phenom*. 2005;142(1):1-25.
6. Roberts S, Beattie I. Micro-Raman spectroscopy in the Earth Sciences. In: Potts PJ, Bowles JFW, Reed SJB, Cave MR, eds. *Microprobe Techniques in the Earth Sciences*. Boston, MA: Springer US; 1995: 387-408.
7. Hofmann S. Sputter depth profiling: Past, present, and future. *Surf Interface Anal*. 2014;46(10–11):654-662.
8. Vickerman JC, Winograd N. SIMS – A precursor and partner to contemporary mass spectrometry. *Int J Mass Spectrom*. 2015;377: 568-579.
9. Moreno-García P, Grimaudo V, Riedo A, et al. Towards structural analysis of polymeric contaminants in electrodeposited Cu films. *Electrochim Acta*. 2016;199:394-402.
10. Russo RE, Mao X, Gonzalez JJ, Mao SS. Femtosecond laser ablation ICP-MS. *J Anal At Spectrom*. 2002;17(9):1072-1075.
11. Zhang B, He M, Hang W, Huang B. Minimizing matrix effect by femtosecond laser ablation and ionization in elemental determination. *Anal Chem*. 2013;85(9):4507-4511.
12. Riedo A, Neuland M, Meyer S, Tulej M, Wurz P. Coupling of LMS with a fs-laser ablation ion source: Elemental and isotope composition measurements. *J Anal At Spectrom*. 2013;28(8): 1256-1269.
13. Russo RE, Mao X, Liu H, Gonzalez J, Mao SS. Laser ablation in analytical chemistry – A review. *Talanta*. 2002;57(3):425-451.
14. Pisonero J, Fernandez B, Gunther D. Critical revision of GD-MS, LA-ICP-MS and SIMS as inorganic mass spectrometric techniques for direct solid analysis. *J Anal At Spectrom*. 2009;24(9):1145-1160.
15. Limbeck A, Galler P, Bonta M, Bauer G, Nischkauer W, Vanhaecke F. Recent advances in quantitative LA-ICP-MS analysis: Challenges and solutions in the life sciences and environmental chemistry. *Anal Bioanal Chem*. 2015;407(22):6593-6617.
16. Laserna J, Vadillo JM, Purohit P. Laser-induced breakdown spectroscopy (LIBS): Fast, effective, and agile leading edge analytical technology. *Appl Spectrosc*. 2018;72(1_suppl):35-50.
17. Wiens RC, Maurice S, Barraclough B, et al. The ChemCam instrument suite on the Mars science laboratory (MSL) rover: Body unit and combined system tests. *Space Sci Rev*. 2012;170(1):167-227.
18. Li Y, Tian D, Ding Y, et al. A review of laser-induced breakdown spectroscopy signal enhancement. *Appl Spectros Rev*. 2018;53(1): 1-35.
19. Lu Y, Zorba V, Mao X, Zheng R, Russo RE. UV fs–ns double-pulse laser induced breakdown spectroscopy for high spatial resolution chemical analysis. *J Anal At Spectrom*. 2013;28(5):743-748.
20. Scaffidi J, Angel SM, Cremers DA. Emission enhancement mechanisms in dual-pulse LIBS. *Anal Chem*. 2006;78(1):24-32.
21. Wang Y, Chen A, Wang Q, et al. Study of signal enhancement in collinear femtosecond-nanosecond double-pulse laser-induced breakdown spectroscopy. *Opt Laser Technol*. 2020;122:1-6, 105887.
22. Bol'shakov AA, Mao X, Russo RE. Spectral emission enhancement by an electric pulse for LIBS and LAMIS. *J Anal At Spectrom*. 2017;32(3): 657-670.
23. Khumaeni A, Akaoka K, Miyabe M, Wakaida I. The role of microwaves in the enhancement of laser-induced plasma emission. *Front Phys*. 2016;11(4):1-7, 114209.
24. Moreno-García P, Grimaudo V, Riedo A, et al. Insights into laser ablation processes of heterogeneous samples: Toward analysis of through-silicon-Vias. *Anal Chem*. 2018;90(11):6666-6674.
25. Cedeño López A, Grimaudo V, Moreno-García P, et al. Towards femtosecond laser ablation ionization mass spectrometric approaches for chemical depth-profiling analysis of lead-free Sn solder bumps with minimized side-wall contributions. *J Anal At Spectrom*. 2018; 33(2):283-293.
26. Tulej M, Neubeck A, Ivarsson M, et al. Chemical composition of micrometer-sized filaments in an aragonite host by a miniature laser ablation/ionization mass spectrometer. *Astrobiology*. 2015;15(8): 669-682.
27. Grimaudo V, Moreno-García P, Riedo A, et al. Review – Laser ablation ionization mass spectrometry (LIMS) for analysis of electrodeposited cu interconnects. *J Electrochem Soc*. 2019;166(1):D3190-D3199.
28. Wiesendanger R, Wacey D, Tulej M, et al. Chemical and optical identification of micrometer-sized 1.9 billion-year-old fossils by combining a miniature laser ablation ionization mass spectrometry system with an optical microscope. *Astrobiology*. 2018;18(8):1071-1080.
29. Neuland MB, Grimaudo V, Mezger K, et al. Quantitative measurement of the chemical composition of geological standards with a miniature laser ablation/ionization mass spectrometer designed for in situ application in space research. *Meas Sci Technol*. 2016;27(3):1-13, 035904.
30. Amoruso S, Bruzzese R, Wang X, O'Connell G, Lunney JG. Multidiagnostic analysis of ultrafast laser ablation of metals with pulse pair irradiation. *J Appl Phys*. 2010;108(11):1-10, 113302.
31. Mildner J, Sarpe C, Götte N, Wollenhaupt M, Baumert T. Emission signal enhancement of laser ablation of metals (aluminum and titanium) by time delayed femtosecond double pulses from femtoseconds to nanoseconds. *Appl Surf Sci*. 2014;302:291-298.
32. Labutin TA, Lednev VN, Ilyin AA, Popov AM. Femtosecond laser-induced breakdown spectroscopy. *J Anal At Spectrom*. 2016;31(1): 90-118.
33. Povarnitsyn ME, Andreev NE, Apfelbaum EM, et al. A wide-range model for simulation of pump-probe experiments with metals. *Appl Surf Sci*. 2012;258(23):9480-9483.
34. Tulej M, Wiesendanger R, Riedo A, Knopp G, Wurz P. Mass spectrometric analysis of the mg plasma produced by double-pulse femtosecond laser irradiation. *J Anal At Spectrom*. 2018;33(8):1292-1303.
35. Riedo A, Bieler A, Neuland M, Tulej M, Wurz P. Performance evaluation of a miniature laser ablation time-of-flight mass spectrometer designed for in situ investigations in planetary space research. *J Mass Spectrom*. 2013;48(1):1-15.
36. Riedo A, Tulej M, Rohner U, Wurz P. High-speed microstrip multi-anode multichannel plate detector system. *Rev Sci Instrum*. 2017;88 (4):1-16, 045114.
37. Rohner U, Whitby JA, Wurz P. A miniature laser ablation time-of-flight mass spectrometer for in situ planetary exploration. *Meas Sci Technol*. 2003;14(12):2159-2164.
38. Wurz P, Lykke KR, Pellin MJ, Gruen DM, Parker DH. Characterization of fullerenes by laser-based mass spectrometry. *Vacuum*. 1992;43(5): 381-385.
39. Hofmann S. Practical surface analysis: State of the art and recent developments in AES, XPS, ISS and SIMS. *Surf Interface Anal*. 1986; 9(1):3-20.
40. Hofmann S. Determination of depth resolution from measured sputtering profiles of multilayer structures: Equations and approximations. *Surf Interface Anal*. 1986;8(2):87-89.
41. Hofmann S. Sputter depth profile analysis of interfaces. *Rep Prog Phys*. 1998;61(7):827-888.
42. Käser D, Hendriks L, Koch J, Günther D. Depth profile analyses with sub 100-nm depth resolution of a metal thin film by femtosecond - laser ablation - inductively coupled plasma - time-of-flight mass spectrometry. *Spectrochim Acta Part B*. 2018;149:176-183.
43. Saghebfar M, Tehrani MK, Darbani SMR, Majd AE. Femtosecond pulse laser ablation of chromium: Experimental results and two-temperature model simulations. *Appl Phys A*. 2016;123(1):1-9, 28.
44. Zhang L, Cao XW, Li SG, Xiang RY, Sun HC. Investigation of femtosecond laser ablation threshold for nickel template. *Appl Mech Mater*. 2014;633–634:665-670.

45. Grimaudo V, Moreno-García P, López AC, et al. Combining anisotropic etching and PDMS casting for three-dimensional analysis of laser ablation processes. *Anal Chem*. 2018;90(4):2692-2700.
46. Grimaudo V, Moreno-García P, Riedo A, et al. High-resolution chemical depth profiling of solid material using a miniature laser ablation/ionization mass spectrometer. *Anal Chem*. 2015;87(4):2037-2041.

How to cite this article: Grimaudo V, Tulej M, Riedo A, et al. UV post-ionization laser ablation ionization mass spectrometry for improved nm-depth profiling resolution on Cr/Ni reference standard. *Rapid Commun Mass Spectrom*. 2020;34:e8803. https://doi.org/10.1002/rcm.8803